Journal of Hazardous Materials 470 (2024) 134156

Contents lists available at ScienceDirect

Journal of Hazardous Materials

journal homepage: www.elsevier.com/locate/jhazmat

Antimony and arsenic migration in a heterogeneous subsurface at an abandoned antimony smelter under rainfall

Chao Li [a,b], Yiyuan Ran [a,c], Pan Wu [c], Peng Liu [d,e], Boyi Yang [f], Xueyuan Gu [f], Ping Zhao [g], Shirong Liu [a], Lei Song [a,b], Yuhui Liu [a], Yizhang Liu [a], Zengping Ning [a], Jing Sun [a,*], Chengshuai Liu [a,*]

[a] State Key Laboratory of Environmental Geochemistry, Institute of Geochemistry, Chinese Academy of Sciences, Guiyang 550081, China
[b] College of Earth and Planetary Sciences, University of Chinese Academy of Sciences, Beijing 101408, China
[c] College of Resources and Environmental Engineering, Guizhou University, Guiyang 550025, China
[d] School of Environmental Studies, China University of Geosciences, Wuhan 430074, China
[e] Hubei Key Laboratory of Yangtze Catchment Environmental Aquatic Science, China University of Geosciences, Wuhan 430074, China
[f] School of Environment, State Key Laboratory of Pollution Control and Resource Reuse, Nanjing University, Nanjing 210023, China
[g] Geological Brigade 105, Guizhou Bureau of Geology and Mineral Exploration and Development, Guiyang 550018, China

HIGHLIGHTS

- Migration of Sb and As in a smelting impacted, stratified subsurface was studied.
- The heterogeneity in permeability caused Sb and As accumulation at the interface.
- Sb and As re-adsorption in the deeper, more acidic layers retarded their migration.
- The Sb mobility was high due to high Sb solid content and ineffective re-adsorption.

GRAPHICAL ABSTRACT

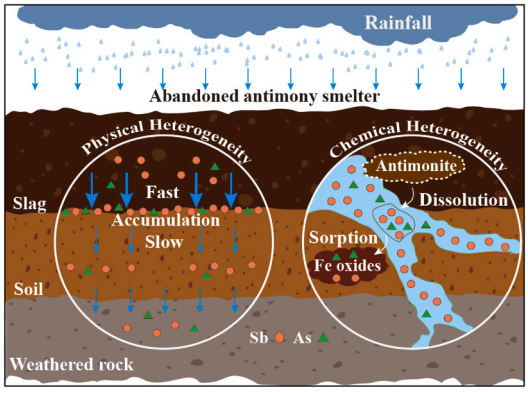

ARTICLE INFO

Keywords:
Sb
As
Physicochemical heterogeneity
Rainfall
Reactive transport modeling

ABSTRACT

While antimony (Sb) and arsenic (As) co-contamination in subsurface soil systems due to the legacy of Sb smelting wastes has been documented, the role of inherent heterogeneity on pollutant migration is largely overlooked. Herein this study investigated Sb and As migration in a slag impacted, vertically stratified subsurface at an abandoned Sb smelter. A 2-dimensional flume was assembled as a lab-scale analogue of the site and subject to rainfall and stop-rain events. Reactive transport modeling was then performed by matching the experimental observations to verify the key factors and processes controlling pollutant migration. Results showed that rainfall caused Sb and As release from the shallow slag layer and promoted their downward movement. Nevertheless, the less permeable deeper layers limited physical flow and transport, which led to Sb and As accumulation at the

* Corresponding authors.
E-mail addresses: sunjing@mail.gyig.ac.cn (J. Sun), liuchengshuai@vip.gyig.ac.cn (C. Liu).

https://doi.org/10.1016/j.jhazmat.2024.134156
Received 27 January 2024; Received in revised form 25 March 2024; Accepted 27 March 2024
Available online 29 March 2024

interface. The re-adsorption of Sb and As onto iron oxides in the deeper, more acidic layers further retarded their migration. Because of the large difference between Sb and As concentrations, Sb re-adsorption was much less effective, which led to higher mobility. Our findings overall highlight the necessity of understanding the degree and impacts of physicochemical heterogeneity for risk exposure assessment and remediation of abandoned Sb smelting sites.

1. Introduction

Due to its chronic toxicity and carcinogenicity, the enrichment of antimony (Sb) in the environment is harmful to humans and organisms [67]. Smelting activities in mining areas are the main source of Sb pollution [5,27]. Because Sb and arsenic (As) have similar geochemical properties and often co-occur in ore deposits, the Sb smelting sites are also typically co-contaminated with As [20,42]. The smelting activities can produce various types of Sb/As-bearing wastes. For example, arsenic-alkali residue is produced during the process of adding alkali to the Sb ore to remove As; desulfurization slag is produced by adding lime water to desulfurize the smelting slag; water-quenched slag is a glassy state material that is formed during rapid water quenching of slag; and the blast furnace ash is the dust that comes out of the flue [25]. These wastes are commonly deposited on the ground surface at the smelter, which releases Sb and As into deeper soils and even groundwater under weathering, mainly as the form of oxyanions [71]. Due to continuous leaching from wastes stacked on the ground surface and/or within soil horizons under rainfall, the degree of contamination at abandoned sites (without new sources) can be similar to that at active smelters [22,36]. Based on investigations at abandoned Sb smelting sites in China that is the world's largest Sb producer, the concentrations of Sb and As can reach thousands and hundreds of mg kg^{-1} in soils, and thousands and hundreds of μg L^{-1} in groundwater [27,67]. The factors and processes regulating the dynamics of Sb and As migration at such sites are essential for accurate risk exposure assessment and for effective remediation, which however have not been well understood.

The migration of solutes in natural soil and groundwater systems are inevitably influenced by the inherent heterogeneity in physical properties [8]. Following different degrees of weathering, the Earth's subsurface especially the unsaturated zone is often vertically stratified with varying particle sizes [4]. Fluid permeability changes with the distribution of different-sized particles, which results in different velocities of the downward flow induced by rainfall and the associated conservative transport behaviors [34]. The fate and transport of potentially toxic metal(loid)s such as Sb and As are further complicated by geochemical properties of the subsurface, which can differ in different layers [60,65,68]. So far, pH, redox potential, and the type and abundance of environmentally relevant minerals such as iron (Fe) and manganese (Mn) oxides have been disclosed to be the main geochemical factors regulating Sb and As mobility [27,60]. While the shallow layer is highly susceptible to human activity, the deeper layers usually possess circumneutral pH, lower redox potential and lower Fe-Mn oxide contents [6,16]. Unfortunately, how the above physicochemical heterogeneities collectively enhance or retard Sb and As migration has not received much attention. Furthermore, a coupled flow, solute and reactive transport modeling approach has been used in recent years to facilitate the understanding of As migration in the subsurface [43]. For instance, Sun et al. [54] and Wallis et al. [56] used reactive transport models to investigate the impact of Fe mineral (trans)formations on groundwater As concentrations in the laboratory and in the field, respectively. Nevertheless, as far as we are aware, no such model is available in the scientific literature that can identify and quantify the contributions of coupled (bio)geochemical and physical processes on the fate of Sb.

In this context, the main objectives were therefore to assess the pollutant release pattern at smelting impacted sites under rainfall and to further elucidate the influences of physicochemical heterogeneity on the rates of Sb and As migration in the subsurface. Soil profiles used in this study were collected from an abandoned Sb smelting site in the Qinglong Sb mine area in China. A 2-dimensional (2D) flume was assembled as a lab-scale analogue of the site, and rainfall events of the study area were replicated in a controlled way. The spatiotemporal evolution of solution composition was determined by collecting and analyzing solution samples from side sampling collectors of the flume. Changes in total concentration and speciation of solid-phase Sb and As as well as other mineralogical changes were also traced using several analytical techniques before and after the experiment. Based on the experimental observations, a coupled flow, solute and reactive transport model was developed, to identify the key processes controlling the behaviors of Sb and As in the heterogeneous subsurface system and to calculate the Sb and As fluxes at the interfaces. The information gleaned from this study is critical to evaluate the fate and transport of Sb and As in the stratified subsurface and to make management decisions regarding the polluted smelting sites.

2. Materials and methods

2.1. Study area and sampling

Our study site is located in Qinglong, Guizhou Province, China (105.15° E, 25.68° N). Qinglong belongs to the subtropical monsoon climate zone, with annual average temperature and rainfall of 14 °C and 1380 mm, respectively [9,61]. With 199,600 tons of Sb mineral reserves, the Qinglong monometallic Sb mine is the third largest Sb mine in China [15,26]. Many smelters were built around the Qinglong mine, including the abandoned smelter in this study [35]. This smelter operated from 1984 to 1991, during which the slag produced was mixed with bricks and stacked on the ground. After 1991, the smelter was abandoned, except for the period between 2013 and 2014 when the local villagers raised flocks, herds, and chickens at the site and in the vicinity. The total area of the abandoned smelter is ~4000 m^2. The elevations of the northern and southern edges are 1850 m and 1650 m above sea level, respectively, with a 6° slope. The groundwater table is buried deep in the study area, > 100 m below the ground surface [63].

A total of 18 sampling locations were selected across the site, and at each location, a soil profile was opened to bedrock (Fig. 1a). Most of the 18 soil profiles could be divided into three layers, which from top to bottom were named as (i) slag layer, (ii) soil layer, and (iii) weathered layer [49]. One sample was collected from each layer at each sampling location, and a total of 54 samples were obtained. The solid samples were brought back to the laboratory within one day of collection and refrigerated at 4 °C in polyethylene sealing bags until experiments or freeze-dried for analysis. The hydraulic conductivities of different layers were measured in the field using an Aardvark type permeameter (Soil-moisture Equipment Corp., USA) [24]. Porewater samples from different layers of the field site were collected periodically over six months using porewater sampler (V_SQR100, China) and filtered to 0.45 μm using polyethersulfone membrane filters (Jin Teng, Tianjin, China). To determine the composition of rainwater in the study area, precipitation was collected. A 1 L polyethylene bottle was placed on the roof and washed three times with the collected rainwater prior to the actual sampling [70]. The collected rainwater was filtered to 0.45 μm using polyethersulfone membrane filters (Jin Teng, Tianjin, China) into polyethylene vials and brought back to the laboratory for analysis.

2.2. Preparation of the flume system

Similar to the experimental apparatus used in Duan et al. [17], a tank mimicking the stratified structure of the field site was assembled for the 2D flume experiment (Fig. 1b). All side walls of the tank were made with acrylic plates. The front wall was drilled with 30 evenly distributed (6 ×5) sampling ports. The left and right walls were perforated. The functioning part of the tank was 40 cm long, 8 cm wide, and 40 cm high. To reduce the flow on the side wall, Vaseline was applied on all side walls of the tank [10]. To simulate the 6° slope of the site and the extremely low permeability of the bedrock, acid-cleaned, high-purity quartz sand (Macklin, AR grade, 16–30 mesh) was placed at the bottom of the tank to form the slope, and a thick rubber mat was placed on top of the quartz sand. The heights of the quartz sand and the rubber mat were 2 cm and 6.2 cm on the left and right sides, respectively. The collected solid samples were then packed into the tank, layer by layer. Each layer was a mixture of the corresponding layer from 18 sampling locations at the field site. Large bricks and weeds were removed before use. An aliquot of each of the three mixtures was removed and analyzed as the pre-experiment solid-phase samples. Each layer had a constant thickness in the tank and was compacted before the next layer was packed. The thicknesses of the slag, soil, and weathered layers were 16 cm, 6 cm and 5 cm, respectively, which were set by reducing the average depths of the corresponding layers of the profiles at the site in proportion to the height of the tank (Text S1 and Fig. S1). Once complete, the tank was stabilized for 24 h.

2.3. Two-dimensional flume experiment with simulated rainfall and sampling

The flume system included the packed tank and a peristaltic pump that was used to simulate rainfall events. 12 channels of peristaltic pump tubing were extended to 8 cm above the tank and fixed, which delivered artificial rainwater (ARW) from the top of the tank. Consistent with the ionic composition and pH of rainwater collected at the site (Table S1), the ARW consisted of distilled water amended with 6 μM Na^+, 10 μM Ca^{2+}, 2 μM Mg^{2+}, 1 μM Cl^-, 5 μM NO_3^-, 2 μM SO_4^{2-} and 20 μM HCO_3^-, and was adjusted to pH 7 with 0.1 M KOH. The flume system was wetted with ARW until the water came out at the bottom, and then the flume experiment started (Day 0). The experiment included three rainfall events and two stop-rain events, to be specific with: (i) rainfall between Day 0 and 24, including a tracer test between Day 4 and 24, (ii) stop-rain between Day 24 and 55, (iii) rainfall between Day 55 and 86, (iv) stop-rain between Day 86 and 156, and (v) rainfall between Day 156 and 176. The rainfall intensity used during periods (i)(iii)(v) was 9 mm day^{-1}, corresponding to the condition of wet season from May to September in Qinglong (see calculation in Text S1). The tracer test was undertaken as part of the experiment to explore the physical transport characteristics within the stratified flume system. The tracer used was bromide (Br), which was added as KBr and amended to the ARW to 0.1 mM.

During the experiment, porewater was periodically collected and analyzed. At each sampling occasion, 2 mL of porewater was collected from each sampling port with a syringe (Fig. 1bc). The collected porewater was filtered to 0.45 μm with a polyethersulfone membrane filter (Jin Teng, Tianjin, China). 1 mL of the filtered sample was acidified to 2% HNO_3 for analysis using inductively coupled plasma mass spectrometry (ICP-MS) and inductively coupled plasma optical emission spectroscopy (ICP-OES). The remaining 1 mL was unacidified and used for ion chromatography (IC) analysis. Following the completion of the experiment on Day 176, solid-phase samples were retrieved from the flume and immediately freeze-dried for subsequent solid-phase analysis. At each side (left, middle or right) of each layer, 3 post-experiment solid-phase samples were collected, and the mean of the obtained data was reported (Fig. S2).

2.4. Analytical procedures

2.4.1. Aqueous analysis

The concentrations of metals in porewater samples from the 2D flume were determined via ICP-MS (Agilent 7700X, USA) and ICP-OES (Agilent WASST-MPX, USA). The concentrations of bromide (Br^-), chloride (Cl^-), nitrate (NO_3^-), nitrite (NO_2^-), fluoride (F^-), and sulfate (SO_4^{2-}) were determined by IC (Dionex ICS-90, USA) with 7.5 mM sodium bicarbonate and 2 mM sodium carbonate as eluents. All these analyses were performed using previously published procedures that demonstrated excellent QA/QC through repeated analysis of certified standards [54,55,57]. For most of our analyzed samples, major ion charges were balanced within 5%.

2.4.2. Bulk solid sample analysis

pH was measured with a solid/water ratio of 1:2.5 by a calibrated pH meter (HQ4300, Hach, USA). Bulk density was calculated based on the physical dimension and weight. Particle size distribution was determined by laser diffraction (LDM, MALVERN, UK). Mineralogy was determined by X-ray diffraction (XRD, Rigaku SmartLab SE, Japan). The collected XRD patterns were processed in MDI Jade 6 (Materials Data Incorporated) and constituent minerals were identified using the search march method against the JCPDS PDF-2 database. Cation exchange capacity (CEC) was measured using the ammonium acetate method [38]. Elemental composition was determined by HNO_3–HF digestion,

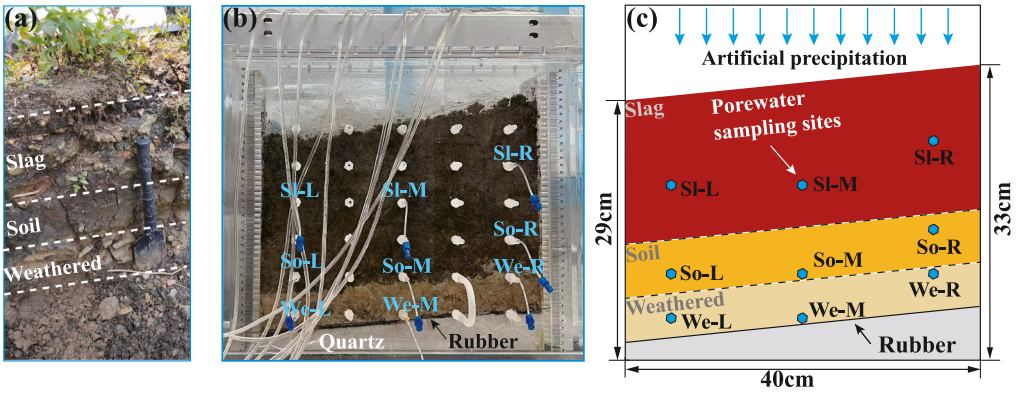

Fig. 1. (a) Digital picture of a representative profile at the field site, which shows stratification with the slag, soil and weathered layers. (b) Digital picture of the front side of the packed 2D flume showing the sampling ports. Porewater sampling was performed using a standard rhizon sampler with a blue head at the selected 9 sampling ports. (c) Schematic diagram of the experimental setup. The different color fills represent different layers. ***Sl, So*** and ***We*** represent the slag, soil and weathered layers, respectively. ***L***, ***M*** and ***R*** represent the left, middle, and right sides of each layer, respectively. The blue hexagonal symbols represent the porewater sampling ports.

followed by analysis via ICP-OES [19].

2.4.3. Solid-phase antimony and arsenic speciation analysis

A five-step sequential extraction procedure was performed on solid-phase samples based on Wenzel et al. [59], followed by analysis via ICP-OES. To perform sequential extraction, 0.2 g of each of the freeze-dried and powdered samples was weighed into a 15 mL centrifuge tube (Corning, USA). Different extraction reagents were added sequentially to extract different fractions of Sb and As, including nonspecifically bound (F1), adsorbed (F2), amorphous (hydr)oxide--bound (F3), crystalline (hydr)oxide-bound (F4), and residual (F5) fraction (details are in Table S2). The suspensions were centrifuged at 4000 rpm for 15 min after each extraction step, followed by the filtration of supernatants through a 0.45 μm filter membrane. The determination of Sb and As in residues was performed using $HCl–HNO_3–HF–H_2O_2$ digestion [19].

The oxidation state of Sb and As was characterized using citric acid extraction method based on Fuentes et al. [23], followed by analysis via atomic fluorescence spectrometry (AFS–97000, Haiguang, Beijing, China). 0.2 g of each sample was placed in a 15 mL centrifuge tube (Corning, USA) and mixed with 10 mL of 100 mM citric acid (pH 2.08). The suspension was stirred at 200 rpm on an orbital shaker for 1 h and then subjected to centrifugation at 4000 rpm for 15 min. The obtained supernatant was filtered through a 0.45 μm polyethersulfone filter membrane (Jin Teng, Tianjin, China). The concentrations of Sb(III) and As(III) were determined directly from the filtered supernatant, since the added citric acid masked the Sb(V) and As(V) signals. Total concentration of Sb was determined after mixing the supernatant with 0.2 mL of 10% thiourea, 0.2 mL of 10% ascorbic acid, 0.2 mL of 1:1 HCl and deionized water that made the sample volume to 2 mL. A similar method was used to determine total As concentration, except that 5% (instead of 10%) ascorbic acid was used. The mixture was allowed to stand for 30 min at room temperature to ensure complete reduction of Sb and As [33]. Sb(V) and As(V) concentrations were then calculated from the differences between total Sb/As and Sb(III)/As(III) concentrations, respectively.

To further determine Sb and As speciation, representative solid-phase samples from the field site were analyzed by X-ray absorption near-edge structure (XANES) spectroscopy. Sb and As K-edge XANES spectra were collected at the Shanghai Synchrotron Radiation Facility on Beamline BL14W1. An aliquot of each freeze-dried, powdered sample was sealed within Kapton tape and analyzed in fluorescence mode, consistent with previously published procedures [21,72]. Energy calibration of Sb and As was ensured by comparing the spectra to the absorption edge of an inline Sb and Au metal foil measured simultaneously with the samples. XANES spectra were processed using ATHENA [47]. Antimonate, antimonite, and stibnite were chosen as Sb references, while arsenate, arsenite, and orpiment were chosen as As references.

2.4.4. Additional morphological and mineralogical analysis

The morphology and elemental composition of the solid-phase samples before and after the experiment were characterized via scanning electron microscopy (SEM, ZEISS Sigma 300, Germany) with energy-dispersive X-ray spectroscopy (EDS, Zeiss SmartEDX). Transmission electron microscopy (TEM, JEOL JEM-F200, Japan) with EDS (Jeol JED-2300 Series) were used to further determine the identity of the Sb/As-bearing minerals.

2.5. Process-based numerical modeling

A coupled flow, solute and reactive transport model was developed to quantitatively interpret the data collected from the 2D flume experiment. Such process-based numerical model integrates the effects of physical flow and transport as well as (bio)geochemical reaction processes, and can be used to identify and quantify the contribution of individual process to the fate of chemicals in subsurface media [48,54]. The construction of this type of models typically involves two stages [43]. The first stage is the development of a flow model and a solute transport model that simulate the behavior of inert species (tracers). The second stage focuses on the development of a conceptual geochemical reaction network and its numerical implementation.

The experimental data collected in this study were simulated using MIN3P-HPC [37]. The versatility of the unstructured grid available in MIN3P-HPC allowed for the inclusion of an angled surface such as the 6° slope of the 2D flume in this study, which could not have been captured adequately using a standard rectangular-based mesh [52]. A total of 2620 triangular meshes with a side length of 0.01 m and a slope of 6° were set in the 2D model (Fig. S3). The boundary conditions included (i) a constant flux boundary at the top, (ii) an outflow boundary on right and left sides, and (iii) a no-flux boundary at the bottom. The total simulation time was set to match the duration of the experiment, i.e., 176 days. The maximum and minimum time steps were 0.176 days and 1.76×10^{-8} days, respectively, as derived from the default settings of MIN3P.

The flow model was set to be a transient, variably saturated model with a recharge rate of 9 mm day^{-1}. The parameters used in the flow model mainly included hydraulic conductivity and Van Genuchten soil hydraulic function parameters (Table 1). Hydraulic conductivity of each layer was initially estimated based on measured particle size distribution and allowed to deviate during the model calibration process. The parameters in Van Genuchten soil hydraulic function for each layer were calculated based on measured particle size distribution and bulk density using neural network prediction in HYDRUS-1D [51]. On the basis of the computed flow field, subsequent conservative transport simulations were performed. Conservative transport parameters included porosity, diffusion coefficients and dispersivity. Porosity was calculated based on the measured bulk density and not varied during model calibration [40]. The diffusion coefficients and dispersivity were determined as part of the model calibration process. Measured [Br] provided the most valuable calibration data for these parameters.

After a good understanding of flow and conservative transport processes was developed, the model was extended to analyze the reactive transport behavior. Based on the experimental observations, a mixture of thermodynamically and kinetically controlled reaction network was defined in the reaction database and successively refined. The mineralogy considered in the model was simplified to only include the minerals effective in dictating porewater chemistry during the experiment.

Table 1
Physicochemical properties of the solids used in the 2D flume experiment.

Properties			Layer		
			Slag	Soil	Weathered
Physical	Bulk density (g cm^{-3})		1.03	1.11	1.20
	Particle distribution	Sand (%)	42.1%	30.1%	27.8%
		Silt (%)	48.1%	57.7%	58.2%
		Clay (%)	9.8%	12.2%	14.0%
	Hydraulic conductivity (m day^{-1})		4.25	0.52	0.48
	Parameters of VG model	θr (cm^3 cm^{-3})	0.044	0.045	0.048
		θs (cm^3 cm^{-3})	0.388	0.340	0.346
		α (cm^{-1})	0.008	0.009	0.008
		n	1.581	1.523	1.539
		l	0.5	0.5	0.5
Chemical	pH		7.3	5.6	6.1
	CEC (cmol kg^{-1})		19.2	12.3	5.0
	Total concentration	Sb (mg kg^{-1})	11,258	473	121
		As (mg kg^{-1})	657	28	13
		Ca (mg kg^{-1})	37,441	3483	1061
		Fe (mg kg^{-1})	44,867	57,482	15,187

The reaction network primarily included three aspects: (1) the dissolution/precipitation of Sb/As-bearing minerals; (2) the adsorption/desorption of Sb/As oxyanions on Fe(III) oxides, and (3) the cation exchange process to account for the evolution of cations in the porewater. In the following, we provide the details for these three aspects of the employed reaction network and describe how the relevant processes were implemented in the model. All other reactions remained consistent with the default database *minteq.dat* from MIN3P-HPC.

Based on characterization results in this study as shown below, calcium antimonite ($Ca[Sb(OH)_6]_2$) and calcium arsenate ($Ca_3(AsO_4)_2$) were assumed to be the main Sb and As-bearing minerals, respectively, in the model. Consistently, a previously published study on this abandoned smelting site showed that Sb in the solid-phase samples was primarily $Ca[Sb(OH)_6]_2$ [69]. The Sb/As-bearing minerals were allowed to dissolve and/or precipitate following the standard first-order rate expression [41]:

$$r = -k \times (1 - SR) \quad (1)$$

where k is the effective rate coefficients; and SR is the saturation ratio, which determines the reaction direction and accounts for the dependence of reaction rate on the dynamically changing geochemical conditions. The equilibrium constants of $Ca[Sb(OH)_6]_2$ and $Ca_3(AsO_4)_2$ were sourced from Cornelis et al. [12] and *minteq.v4.dat*, respectively (Table S3). The amounts of $Ca[Sb(OH)_6]_2$ and $Ca_3(AsO_4)_2$ used in the model were set based on total Sb and As concentrations from digestion. The effective rate coefficients were subject to model calibration.

Owing to the high affinity of Sb and As oxyanions for mineral surfaces, adsorption/desorption process plays a key role in regulating the migration of Sb and As [53,54]. Iron oxides were previously found to provide the main surface for Sb adsorption in solid samples from this study site [69]. Therefore, sorption of anions (e.g., Sb and As) and cations (e.g., Fe^{2+} and Ca^{2+}) was assumed to occur on Fe oxides as surface complexation reactions, consistent with our previously published models [48,54]. The surface complexation model was included based on Dzombak and Morel [18] with reactions:

$$FeOH + A^- + H^+ \leftrightarrow FeOH_2 - A \quad (2)$$

where $FeOH$ and A^- represent the Fe oxide surface and adsorbate, respectively. The stoichiometry and thermodynamic constants were from *minteq.v4.dat* (Table S3). Consistent with Zhao et al. [69], the surface site masses were assumed to be 250 g L^{-1}, 250 g L^{-1} and 150 g L^{-1} in the slag, soil and weathered layers, respectively. Consistent with Demers et al. [13], the specific surface area and site density of Fe oxides were set to be 300 m^2 g^{-1} and 5 sites nm^{-2}, respectively.

A cation exchange site (X) was also implemented in the model. The reactions between the X site and cations could be expressed as:

$$Cat^{+i} + iX^- \leftrightarrow CatX_i \quad (3)$$

where Cat^{+i} represent cations including Na^+, K^+, Ca^{2+}, Mg^{2+} and Fe^{2+}. The cation exchange capacities set in the model were derived from CEC measurements, which were 19.2 cmol kg^{-1}, 12.3 cmol kg^{-1}, and 5.0 cmol kg^{-1} for the slag, soil, and weathered layers, respectively (Table 1).

The model refinement and associated improved agreement between observations and model-simulation equivalents were achieved by a parameter estimation procedure. The process began with manual trial-and-error calibration, followed by automatic calibration using the Gauss–Levenberg–Marquardt method contained in PEST++ [58]. As detailed above, model parameters to be calibrated included hydraulic conductivity, diffusion coefficients, dispersivity, as well as effective rate coefficients of mineral dissolution/precipitation reactions (Table 1 and S3). Measured spatiotemporal porewater compositions comprised the primary calibration dataset. The procedure of weight assignment during automatic calibration was adopted from Sun et al. [54], and based on the magnitude of each measurement, the number of measurements available, and the uncertainty inherent in each measurement type.

3. Results

3.1. Physicochemical heterogeneity

At our Qinglong field site, the subsurface system above bedrock was stratified from top to bottom (Fig. 1a). Such stratification was well replicated in the 2D flume (Fig. 1b). Three layers (i.e., slag, soil and weathered layer) could be identified based on physicochemical properties (Table 1). The slag layer was black-brown and contained a mixture of water-quenched slags from Sb fire smelting method and bricks. The soil layer was made of natural yellow-brown soil. The weathered layer was adjacent to the bedrock and was brown. In the field, the hydraulic conductivity of the slag layer was determined to be 9.24–24.19 m day^{-1}; the hydraulic conductivities of the soil layer and the weathered layer were similar and around 0.46–0.92 m day^{-1}. The bulk density also varied slightly from layer to layer. For the field samples, the bulk density of the slag layer was 1.04–1.12 g cm^{-3}; the bulk density of the soil layer and the weathered layer were 1.10–1.18 g cm^{-3} and 1.13–1.24 g cm^{-3}, respectively. The slag layer was mildly alkaline (pH 7.1–8.7) across the field site, owing to the influence of the Sb fire smelting method. In contrast, the soil and weathered layers remained acidic with pH ranging between 4.4 and 6.3 at the site.

The individual layers from 18 profiles at the field site were mixed and homogenized before used in the 2D flume. The bulk density of the homogenized slag, soil and weather layer were 1.03 g cm^{-3}, 1.11 g cm^{-3} and 1.20 g cm^{-3}, respectively, consistent with those determined on field samples (Table 1). The proportion of sand particles (i.e., 0.02–2 mm) was the highest (42.1%) in the slag layer and the lowest (27.8%) in the weathered layer (Table 1). Although the particle size generally became finer with increasing depth, the particle size distributions in the soil and weathered layers were similar. pH in the assembled 2D flume also decreased from 7.3 in the slag layer to 5.6 and 6.1 at depth (Table 1). Based on XRD, bulk mineralogy of all three layers was dominated by quartz. Calcite and dolomite were identified in the slag layer but were not detected in the other layers (Fig. S4).

Based on digestion, total concentrations of Sb in the slag, soil and weathered layers were 11,258 mg kg^{-1}, 473 mg kg^{-1} and 121 mg kg^{-1}, respectively (Table 1). In comparison, the concentrations of As were much lower, being 657 mg kg^{-1}, 28 mg kg^{-1} and 13 mg kg^{-1} in the slag, soil and weathered layers, respectively. These concentrations show that this abandoned smelting site is severely polluted, since the geological background values of Sb and As in Qinglong are only 2.2 mg kg^{-1} and 20.0 mg kg^{-1}, respectively [35]. Total concentration of Ca in the slag layer was substantially higher than those in the soil and weathered layers, at least partially due to the presence of calcite and dolomite as verified by XRD (Fig. S4 and Table 1). Total concentrations of Fe in the slag and soil layers were much higher than that in the weathered layer (Table 1). The concentrations of Sb and As were both positively correlated with Ca, with Spearman's coefficients being 0.617 and 0.500, respectively (Table 2). In comparison, the correlation between Sb/As and Fe was less significant (Table 2). TEM/SEM-EDS showed consistent results with bulk digestion (Fig. 2 and S5). Positive

Table 2
Spearman's coefficients between Sb, As, Ca, and Fe concentrations of the slag layer, as measured by digestion (outside the parentheses) and SEM-EDS (between parentheses).

	Sb	As	Ca	Fe
Sb	1			
As	0.767 * (0.282)	1		
Ca	0.617 (0.609 *)	0.500 (0.616 *)	1	
Fe	0.467 (0.648 *)	0.400 (−0.014)	-0.083 (0.084)	1

Note: * indicates $p < 0.05$.

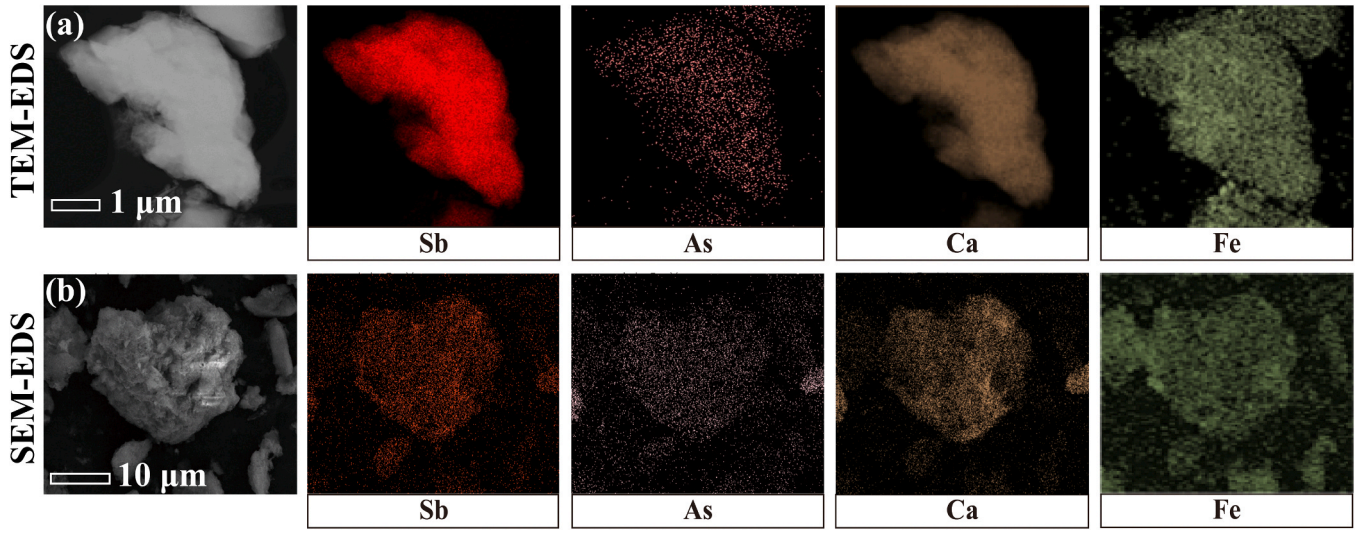

Fig. 2. (a) TEM and (b) SEM images of representative solid samples collected from the slag layer and the distributions of Sb, As, Ca and Fe. Additional images are in Fig. S5.

correlations were also observed between the concentrations of Sb/As and Ca using SEM-EDS, with Spearman's coefficients being 0.609 and 0.616, respectively (Table 2). Both citric acid extractions (Fig. 3) and XANES (Fig. S6) showed that Sb and As in all three layers were dominated by + 5 valence. It was therefore speculated that the mineral forms of Sb and As were mainly $Ca[Sb(OH)_6]_2$ and $Ca_3(AsO_4)_2$, respectively, although no Sb- or As-bearing minerals could be identified by XRD because those minerals, if present, were in trace quantities (Fig. S4). As suggested by sequential extraction, almost all of the Sb in the slag layer was in residual fraction (F5), whereas 23.6% and 51.5% were present as extractable Sb (F1–4) in the soil and weathered layers, respectively (Fig. 3). Unlike Sb, As was dominated by the residue fraction in all three layers.

3.2. Tracer breakthrough characteristics

0.1 mM of Br tracer was added in the artificial rainfall as a pulse between Day 4 and 24 in the 2D flume experiment. Accordingly, porewater [Br] in each layer increased and then decreased (Fig. 4a). Br was detected in porewater of the slag layer immediately after addition, and sequentially in the deeper soil and weathered layers. In the slag layer, porewater [Br] peaked at 0.11 mM on Day 20, gradually decreased to 0.08 mM on Day 55 and dropped to undetectable value on Day 80. In the soil and weathered layers, porewater [Br] started to increase on Day 8, peaked at 0.04 mM on Day 20, and became undetectable on Day 164. The slope of the Br breakthrough curve was steep in the slag layer and much smoother in the soil and weathered layers (Fig. 4a). The observed porewater [Br] provided valuable information for the calibration of the flow and conservative transport model, and good agreements were achieved between observed data and simulated equivalents (Fig. 4a). The Darcy flow velocities in the slag, soil and weathered layers under rainfall were estimated to be ~0.010 m day^{-1}, 0.003 m day^{-1} and 0.001 m day^{-1}, respectively, consistent with the observed different Br migration rates in different layers (Fig. 5a). Based on the model, water in the 2D flume only flowed downward under rainfall, i.e., periods (i)(iii)(v), and remained still during stop-rain events, i.e., periods (ii)(iv) (Fig. 5a). The modeling results further showed that under rainfall, the direction of the water flow changed from vertically downward to partially lateral at the slag/soil interface (Fig. S7).

3.3. Antimony and arsenic release and accumulation

The 2D flume experiment induced Sb and As release into the porewater (Figs. 4bc and 5cd) and re-distributed Sb and As in the solid-phase (Fig. 3). In the slag layer, porewater [Sb] increased slowly to ~0.07–0.09 mM during the 1st rainfall event, further increased to ~0.10–0.12 mM during the 2nd rainfall event and decreased gradually to ~0.07–0.10 mM during the 3rd rainfall event. Porewater [Sb] in the soil and weathered layers were essentially unchanged at ~0.02 and 0.005 mM, respectively (Fig. 4b). Solid Sb concentration decreased to 8899 ± 1836 mg kg^{-1} in the slag layer, but increased to 769 ± 160 mg kg^{-1} and 153 ± 38 mg kg^{-1} in soil and weathered layers, respectively (Fig. 3). Porewater [As] remained stable across all three layers under rainfall (Fig. 4c). Porewater [As] was ~0.01 mM in the slag layer, while it was 2 orders of magnitude lower in the soil and weathered layers. The variations in solid As concentrations before and after the experiment were similar to those in Sb concentrations, which decreased to 303 ± 113 mg kg^{-1} in the slag layer but increased to 41 ± 5 mg kg^{-1} and 13 ± 2 mg kg^{-1} in the soil and weathered layers, respectively (Fig. 3). Porewater [Sb] and [As] at the field site were comparable to porewater [Sb] and [As] from the 2D flume experiment (Fig. S8). In the field, porewater [Sb] and [As] in the slag layer were also relatively high, and the differences between concentrations in the soil and weathered layers were subtle.

Sequential extractions and citric acid extractions were conducted on the solid samples before and after the flume experiment to monitor the alterations in Sb and As speciation (Fig. 3). The results showed that the experiment did not change the geochemical fractionation of Sb in the slag layer, which was still dominated by the residual fraction (F5), but increased the fraction of extractable Sb (F1–4) in the soil and weathered layers (Fig. 3). More specifically, the fraction of adsorbed Sb (F2) increased from 0.2% to 4.1% in the soil layer and from 0.1% to 2.2% in the weathered layer. The fraction of amorphous/crystalline (hydr)oxide-bound Sb (F3–4) in the soil and weathered layers increased from 22.3% to 39.7% and from 50.3% to 67.1%, respectively. Besides fraction, the total amount of extractable Sb (F1–4) by sequential extraction decreased from 71.7 to 25.6 mg kg^{-1} in the slag layer. The amount of extractable Sb by citric acid, on the other hand, increased from 735 to 1005 mg kg^{-1}, while Sb remained as Sb(V) in the slag layer (Fig. 3). The experiment did not cause noticeable changes in the concentrations and proportion of Sb(V) and Sb(III) in the soil layer, with concentrations being 65.9 mg kg^{-1} and 4.4 mg kg^{-1}, respectively. The concentration of Sb(III) in the weathered layer increased from 0.8 mg kg^{-1} to 2.4 mg kg^{-1}, and its proportion increased from 6.3% to 20.8% (Fig. 3). Similar to Sb, As in the slag layer remained all in the residual fraction. The fraction of adsorbed As (F2) in the soil and weathered layers

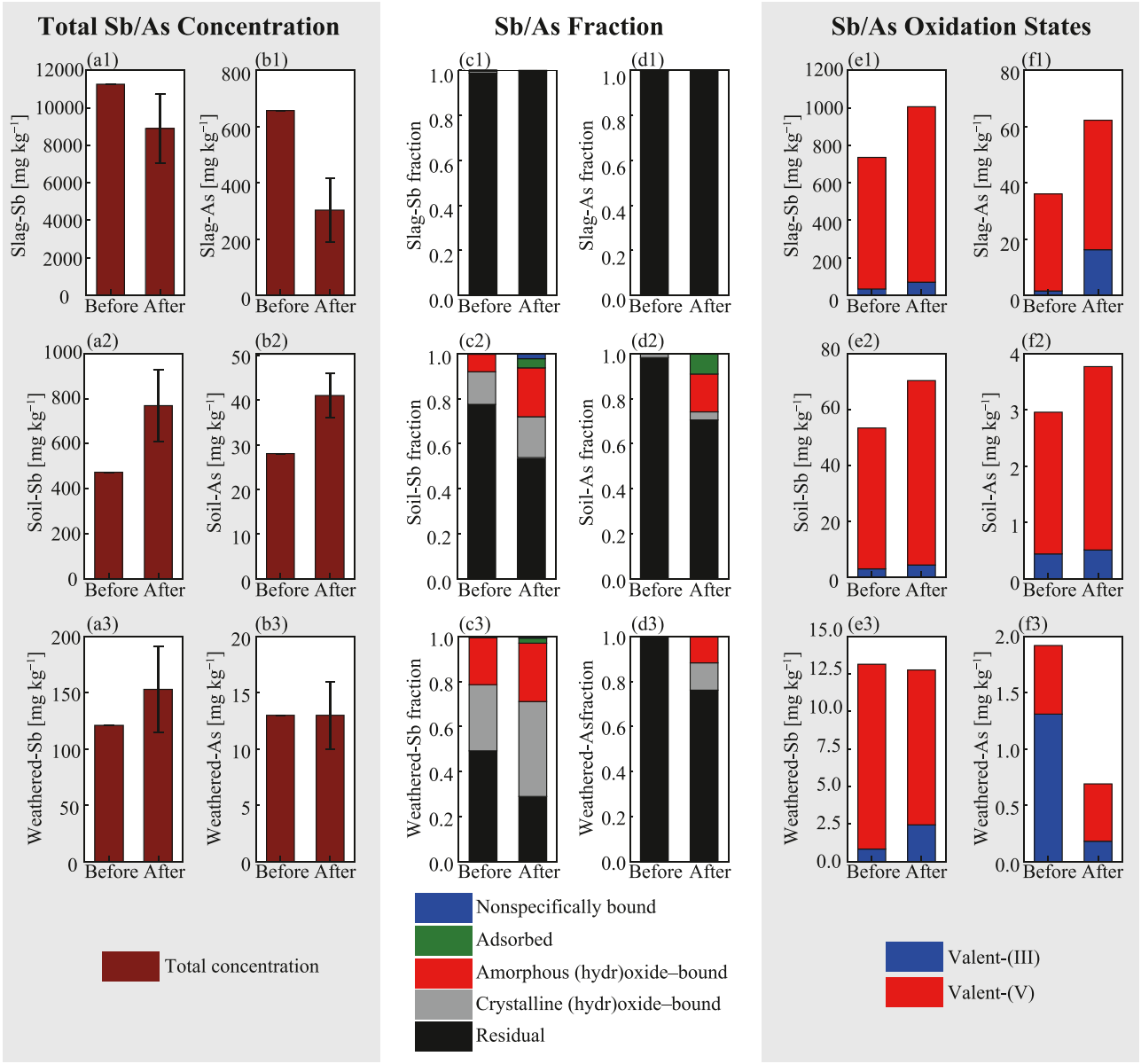

Fig. 3. (a1-a3 & b1-b3) Total concentration, (c1-c3 & d1-d3) sequential extraction results and (e1-e3 & f1-f3) oxidation states from citric acid extraction of Sb and As in the slag, soil and weathered layers before and after the experiment.

increased from 0.0% to 9.1% and from 0.0% to 0.5%, respectively. The amorphous/crystalline (hydr)oxide-bound As (F3–4) increased from 1.7% to 19.8% and from 0.0% to 23.8% in the soil and weathered layers, respectively (Fig. 3). The biggest change in As oxidation state occurred in the slag layer, with As(III) concentration increasing from 1.5 mg kg^{-1} to 16.2 mg kg^{-1} and proportion increasing from 0.4% to 26.1%. The concentrations and proportions of As(V) and As(III) in the soil layer did not change much, with concentrations being 3.26 mg kg^{-1} and 0.51 mg kg^{-1}, respectively. As for the weathered layer, As(V) concentration stayed around 0.5 mg kg^{-1}, but As(III) concentration reduced from 1.31 mg kg^{-1} to 0.18 mg kg^{-1}, and As(III) proportion reduced from 87.9% to 54.5% (Fig. 3).

Reactive transport behaviors of Sb and As during the 2D flume experiment, as deduced from the observations, could be described with a relatively simple conceptual/numerical model (Fig. 4). The variations in solid Sb/As concentrations before and after the experiment could be well replicated by considering the dissolution of Sb/As containing minerals such as $Ca[Sb(OH)_6]_2$ and $Ca_3(AsO_4)_2$ in slag layer under rainfall, and the subsequent migration of the released Sb and As with water flow to the underlying soil and weathered layers. The transport of Sb and As was mainly retarded by re-adsorption on the surface of Fe oxides in the soil and weathered layers, resulting in increases in the adsorbed (F2) and (hydr)oxide-bound (F3–4) Sb/As fractions after the experiment (Fig. 3). Average Sb and As downward fluxes were calculated using the model, which showed that Sb and As cross-interface transport occurred only during rainfall events (Fig. 6). The Sb fluxes at the two interfaces varied by an order of magnitude, being 0–9.5 mM day^{-1} and 0–0.4 mM day^{-1} at the slag/soil and soil/weathered interfaces, respectively. In comparison, the As fluxes were much lower and varied by 2 orders of magnitude at the two interfaces, being 0–0.1 mM day^{-1} and 0–0.001 mM day^{-1}, respectively.

3.4. *Evolution of porewater cation concentrations*

The temporal evolution of porewater cation composition was also determined during the experiment and simulated by the numerical model. A characteristic feature of the observed breakthrough behavior of Ca is that despite the positive correlation between solid Ca and Sb

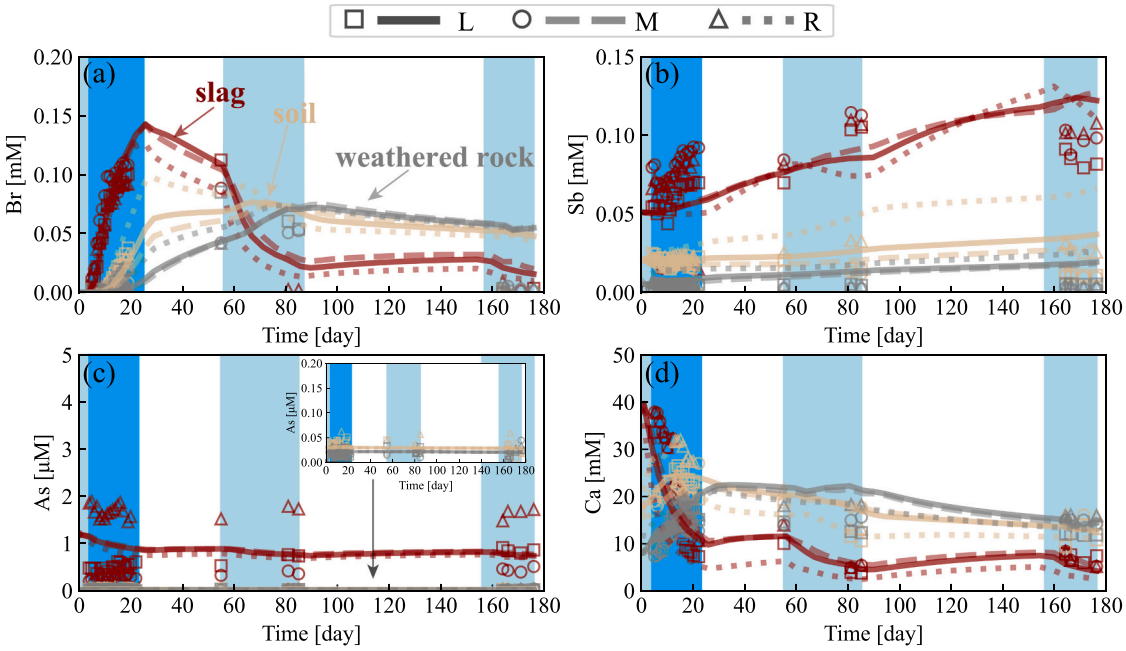

Fig. 4. Porewater (a) [Br], (b) [Sb], (c) [As] and (d) [Ca] versus time during the experiment. Observations are plotted as symbols, while simulations are plotted as lines. The blue and white backgrounds represent rainfall and stop-rain events, respectively. The dark blue background represents the period during which KBr tracer was added to the rainwater. ***L***, ***M*** and ***R*** in the legend represent the left, middle and right sampling ports in each layer, respectively.

concentrations in the slag layer, porewater [Ca] showed a negative correlation with porewater [Sb] (Fig. 4bd). Porewater [Ca] in the slag layer decreased rapidly from 40 mM to 8 mM during the 1st rainfall event, kept decreasing but much more gradually during the other two rainfall events, and eventually decreased to 5 mM at the end of the experiment. Porewater [Ca] in the soil layer showed an increasing and then decreasing trend under rainfall. Specifically, [Ca] increased from 28 mM to 33 mM during Day 4–18 and decreased to 15 mM during Day 18–176. Porewater [Ca] in the weathered layer displayed a similar trend, which increased from 10 mM to 17 mM during Day 4–18 and decreased to 10 mM during Day 18–176. Porewater [Mg] in the experiment mirrored the responses in [Ca] (Fig. S9a). Slight increases in porewater [Ca] and [Mg] were observed at the start of the 2nd rainfall event compared to the end of the 1st one, after a month of hiatus. All these observations could be well reproduced by the developed reactive transport model after considering cation exchange process (Fig. 4d and S9a).

4. Discussion

4.1. Effects of physical heterogeneity

Three layers with varying particle sizes exist at our field site and its lab-scale analogue (Fig. 1). The heterogeneity in particle size can cause distinct physical flow and transport characteristics [66]. Constrained by observations from the 2D flume experiment, hydraulic conductivities of the slag, soil and weathered layers were estimated to be 4.25 m day^{-1}, 0.52 m day^{-1} and 0.48 m day^{-1}, respectively (Table 1). The greater the hydraulic conductivity, the shorter the penetration time of the solute, and subsequently the steeper the breakthrough curve [30]. Accordingly, in the 2D flume experiment, Br breakthrough curve in the slag layer had a steeper slope compared to those in the soil and weathered layers (Fig. 4a). The relatively low hydraulic conductivity of the soil layer can limit pollution from spreading to the surrounding environment [64]. To demonstrate the role of hydraulic conductivity, a model variant was constructed on the basis of the final calibrated model, in which the hydraulic conductivity of the soil layer was adjusted. With a 10–fold increase in hydraulic conductivity, the downward migration of Sb under rainfall was substantially promoted, with Sb fluxes increasing from 0–9.5 mM day^{-1} to 0–13.2 mM day^{-1} at the slag/soil interface and from 0–0.4 mM day^{-1} to 0–0.5 mM day^{-1} at the soil/weathered interface (Fig. 6 and S10). Similar with Sb, As fluxes increased from 0–0.1 mM day^{-1} to 0–0.22 mM day^{-1} at the slag/soil interface, while remained unchanged at the soil/weathered interface (Fig. 6 and S10), because the transport of As was substantially retarded by re-adsorption onto Fe oxides in the soil layer as discussed later. Changes in rainfall intensity may also impact the migration of Sb and As. To study the influence of rainfall intensity on Sb and As downward transport, two model variations were created based on the calibrated model, with adjustments made to the recharge rate (Fig. 6 and S10). With a 5–fold increase in recharge rate that mimics intense rainfall, the downward Sb fluxes increasing from 0–9.5 mM day^{-1} to 0–27.6 mM day^{-1} at the slag/soil interface and from 0–0.4 mM day^{-1} to 0–4.5 mM day^{-1} at the soil/weathered interface. The downward As fluxes increased from 0–0.1 mM day^{-1} to 0–0.19 mM day^{-1} at the slag/soil interface and again remained unchanged at the soil/weathered interface. With a 5–fold decrease in recharge rate that mimics the dry season, the fluxes decreased substantially. The downward Sb fluxes were only 0–0.45 mM day^{-1} and 0–0.05 mM day^{-1} at the slag/soil interface and the soil/weathered interface, respectively. The downward As fluxes decreased to almost 0 mM day^{-1} at both interfaces.

Due to the difference in hydraulic conductivity between the slag and soil layers, downward flow induced by rainfall events could not freely cross their interface, which could lead to deviation in flow direction and accumulation of solutes [62]. Accordingly, the modeling results showed that flow direction changed from straight downward to partially leftward at the slag/soil interface (Fig. S7) and Sb/As accumulated there (Fig. 5 cd). Such phenomenon is similar to the findings of previous studies with stratified subsurface systems, including salt accumulation in the interfacial clay-rich layers in agricultural plots in Purandara et al. [44] and As accumulation on top of the clay lenses in the 2D flume in Duan et al. [17]. Additionally, porewater [Ca] in the slag layer increased slowly from ~6 mM to ~7 mM during the 1st stop-rain event, possibly also because the difference in hydraulic conductivity between the slag and soil layers caused back-diffusion [62]. Moreover, due to the larger particle size, the slag layer possesses more voids and channels, which

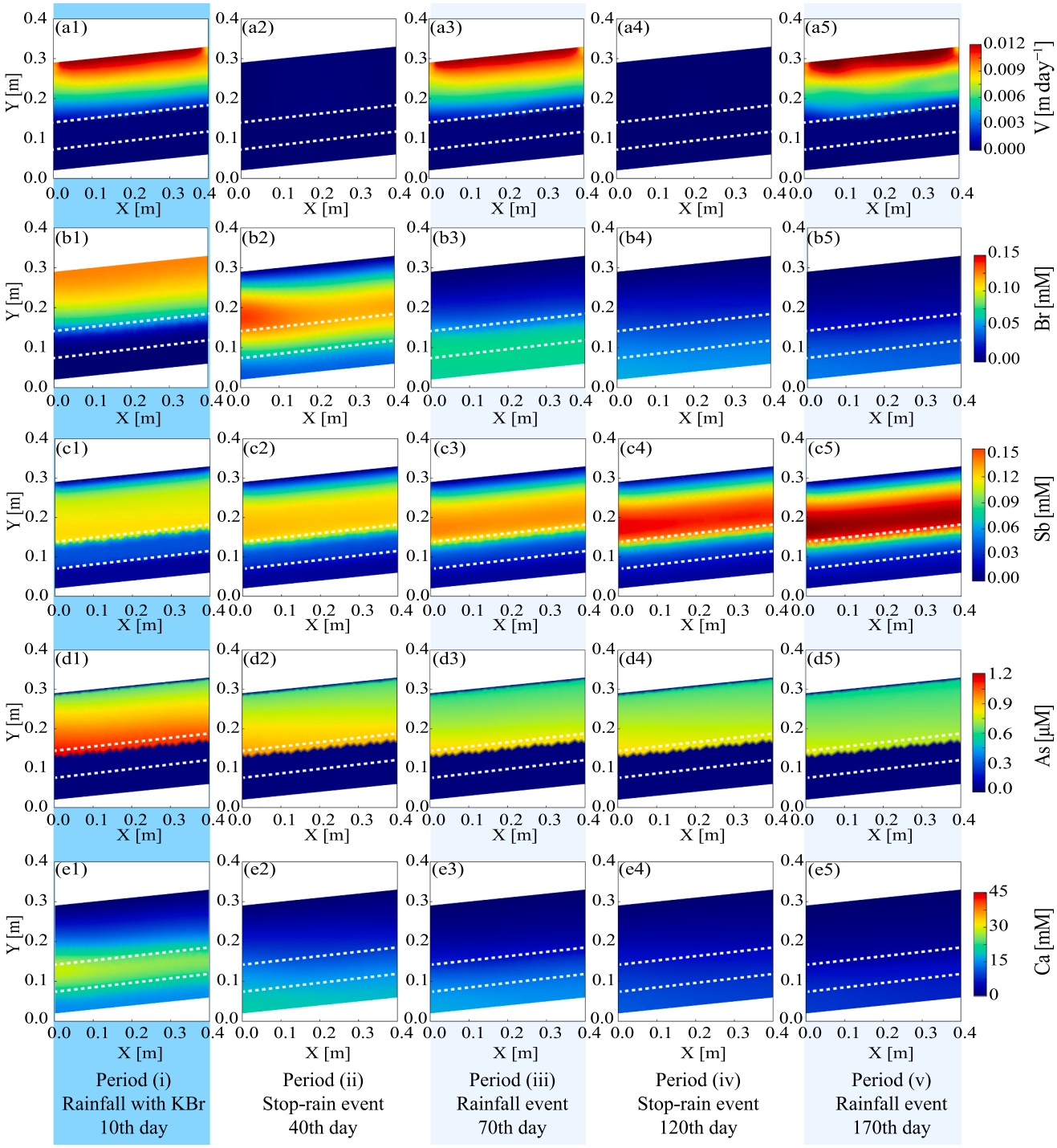

Fig. 5. Simulated flow field, and porewater [Br], [Sb], [As], and [Ca] in the 2D flume during experimental period i (Day 10), ii (Day 40), iii (Day 70), iv (Day 120) and v (Day 170). The two white dashed lines in each subplot represent the slag/soil and soil/weathered interfaces.

tend to form fast flow paths and accelerate solute advection [39]. Consequently, despite varying depths of the three subsampling ports within the slag layer, observed porewater [Br] were all the same (Fig. 4a). In contrast, the soil and weathered layers have finer particle sizes and thereby fewer fast flow channels [31]. In the soil and weathered layers, since the middle subsampling ports were deeper compared to the ports on the left and right sides, porewater [Br] at the middle was lower (Fig. 4a). All the aforementioned physical heterogeneity and the associated flow and transport processes also regulated the fate of Sb and As, although chemical heterogeneity impacted their breakthrough at least equally strongly as elaborated below.

4.2. *Effects of chemical heterogeneity*

The subsurface system at our Qinglong field site and its corresponding 2D flume possess strong chemical heterogeneity in the vertical direction (Table 1). The large differences between solid-phase Sb/As concentrations in each layer led to substantial differences in their corresponding porewater concentrations (Fig. 4bc) and cross-interface fluxes (Fig. 6). In the flume experiment, the highest Sb and As concentrations were found in the solids and porewater of the slag layer, followed by the soil layer and the lowest in the weathered layer. Furthermore, pH, which is a key factor affecting the solubility and

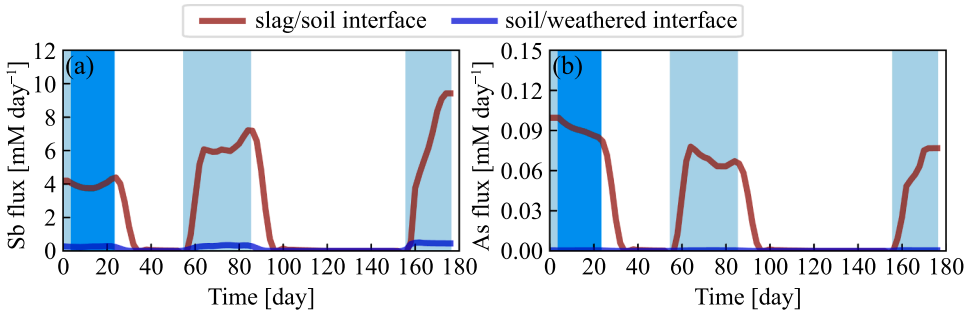

Fig. 6. Calculated fluxes of (a) Sb and (b) As at the interfaces between the slag and soil layers and between the soil and weathered layers, respectively.

mobility of Sb and As [45], also varied in the vertical direction. The smelting operation at this now abandoned Sb smelter used alkaline leaching solution to purify Sb and produced alkaline slags [3]. Accordingly, the slag layer was alkaline at the site and in the flume, whereas the soil and weathered layers were more acidic (Table 1). A more acidic environment would enhance adsorption of Sb and As on Fe oxides, as they mainly existed in our system as negatively charged $Sb(OH)_6^-$ and $H_2AsO_4^-$, respectively [11,46]. Accordingly, compared to the slag layer, the soil and weathered layers contained higher fractions of the adsorbed (F2) and (hydr)oxide-bound (F3–4) Sb and As, both before and after the flume experiment (Fig. 3). In addition, observed porewater [As] on the right side of the slag layer were noticeably higher (Fig. 4d). On the contrary, simulated porewater [As] was lower on the right side, because the layers in the 2D flume were inclined 6° to the upper right, and the associated flow direction was towards the lower left corner (Fig. S7). The opposite behaviors between observation and simulation are interpreted to be a result of subtle chemical heterogeneity in the lateral direction. Although the solids were homogenized by manual mixing before packing into the 2D flume, heterogeneity could easily exist [2]. In the slag layer, the amount of leachable As in the solids was probably higher on the right side, which released more As under rainfall.

Besides the above spatial heterogeneities, large difference between the absolute amounts of Sb and As existed at this abandoned smelting site and considerably affected their release and migration patterns. Since the Qinglong Sb mine is monometallic [49], the solid samples in this study contained 9–17 fold more Sb than As (Table 1). Nevertheless, porewater [Sb] in the experiment were 50–100 fold higher than [As] (Fig. 4bc). The ratio of porewater [Sb] to the amount of solid Sb was therefore 3–10 fold larger (Fig. S11), indicating a higher mobility of Sb. The different mobilities between Sb and As might be partially due to the experimental settings of rainfall and stop-rain events, as previous studies found that alternating wet and dry conditions are more favorable for Sb leaching, whereas As is more readily leached under full immersion [7,32]. Nevertheless, based on the combination between observations and modeling results, this difference could in fact mainly be attributed to the substantial difference between the absolute amounts of Sb and As. In contrast to As, the amount of Sb mobilized from the slag layer was too high to be effectively re-sequestered during downward transport (Fig. 4bc) [14]. Consequently, calculated cross-interface Sb fluxes were ~2 orders of magnitude larger than As fluxes (Fig. 6).

4.3. Additional characteristics of the fates of antimony and arsenic

Under long-term weathering, reactive Sb and As would gradually enter mineral lattices and thereby transform into recalcitrant forms [1,28]. Accordingly, pre-experiment Sb and As in the slag layer were both dominated by the residual fraction (F5) (Fig. 3), and only a small fraction of the solid Sb and As was solubilized under rainfall (Fig. 4bc). The solubilized Sb and As from the slag layer were partially re-sequestered by adsorption on Fe oxides in the deeper layers during downward transport (Fig. 3). Although such adsorption process retarded Sb and As migration, it is well known that surface bound Sb and As can be easily re-mobilized [50]. The amounts of Sb and As that could be extracted by citric acid also increased in all three layers after the experiment (Fig. 3). Therefore, the alternating wet and dry conditions induced by rainfall and stop-rain events could increase the reactivities of solid Sb and As from the abandoned smelter, at least over the short-term.

The main Sb- and As-bearing ore minerals in this Qinglong Sb mine are both sulfide minerals, to be specific, stibnite (Sb_2S_3) and arsenopyrite (FeAsS), respectively [9,29]. The Sb smelting process used at this abandoned smelter, on the other hand, would result in the generation of Na_3SbO_3 and Na_3AsO_3 in the slags [3,49]. Nevertheless, based on both citric acid extraction and XANES, Sb was predominantly Sb(V) in pre-experiment samples, whereas the proportion of As with + 3 valence was higher (Fig. 3). The difference in Sb and As oxidation states observed in this study is consistent with the findings from many previous studies, which showed that Sb can be more easily oxidized relative to As under weathering [60,65,68]. Moreover, while Sb remained as Sb(V) during the flume experiment, As(V) reduction to As(III) occurred in the slag layer (Fig. 3). This might be a result of the inundation conditions that developed under rainfall, as the oxidation state of As is more sensitive to alternating wet and dry conditions than Sb [7]. Additionally, it is noteworthy that the amount of As(V) in the deeper layers did not change much but most of the As(III) was leached away (Fig. 3), consistent with the higher mobility of As(III) relative to As(V) [45].

5. Conclusions and implications

This study was motivated by the need to evaluate the fate and transport of two important contaminants, Sb and As, in subsurface systems at Sb smelting sites. A 2D flume experiment was performed with three distinct layers of solids collected from a typical abandoned Sb smelter in Qinglong, China and subject to rainfall and stop-rain events. Combining experimental observations and process-based numerical modeling, this study revealed the similarities and differences in Sb and As behaviors, and especially highlighted the influences of physico-chemical heterogeneity on their migration. Rainfall induced Sb/As release from smelting slags in the shallow layer, yet Sb and As could not freely migrate to the deeper layers due to re-adsorption on Fe oxides. The variations in hydraulic conductivity in the vertical direction caused distinct pollutant migration rates in different layers as well as Sb and As accumulation at the slag/soil interface. Under alternating wet and dry conditions induced by rainfall and stop-rain events in the present study, As was easier to be reduced to more mobile trivalent form. Nevertheless, Sb had a higher mobility relative to As, mainly due to the much higher Sb concentrations.

Based on the calculated downward fluxes of Sb and As in the 2D flume (Fig. 6), the rainfall condition in the study area and the size of the site (~4000 m^2), the Sb and As fluxes at the slag/soil interface at this abandoned Sb smelter could be speculated to be ~10000 mol $year^{-1}$ and 200 mol $year^{-1}$, respectively, using simple extrapolation. Additionally, since the site has a slope of ~6°, the highest levels of porewater [Sb] and

[As] would likely occur at the southwest corner of the site. Nevertheless, because the actual site is much more heterogeneous than the 2D flume, more detailed analysis and modeling of the flow field and the Sb and As reactive transport behaviors will be required for more accurate predictions of Sb and As input and output fluxes at this and other smelting sites.

Environmental implication

The legacy of tailings and wastes from antimony mining and smelting operations can potentially cause elevated concentrations of antimony and arsenic in the environment, which may lead to serious human and ecosystem health concerns. This study focused on antimony and arsenic release and migration in a smelting slag impacted, vertically stratified subsurface under rainfall, using a two-dimensional flume experiment combined with a coupled flow, solute and reactive transport model. The findings highlight the significance of physicochemical heterogeneity on the fate of antimony and arsenic, and will help us make better management decisions regarding the polluted smelting sites.

CRediT authorship contribution statement

Ping Zhao: Writing – review & editing, Resources. **Shirong Liu:** Writing – review & editing, Methodology. **Xueyuan Gu:** Writing – review & editing, Methodology. **Yizhang Liu:** Writing – review & editing, Methodology. **Zengping Ning:** Writing – review & editing, Methodology. **Chao Li:** Writing – original draft, Visualization, Software, Methodology, Data curation. **Lei Song:** Writing – review & editing, Methodology. **Yuhui Liu:** Writing – review & editing, Methodology. **Peng Liu:** Writing – review & editing, Resources, Methodology. **Boyi Yang:** Writing – review & editing, Methodology. **Jing Sun:** Writing – review & editing, Validation, Supervision, Resources, Project administration, Funding acquisition, Conceptualization. **Yiyuan Ran:** Writing – review & editing, Methodology, Data curation. **Chengshuai Liu:** Writing – review & editing, Validation, Supervision, Resources, Project administration, Conceptualization. **Pan Wu:** Writing – review & editing, Methodology.

Declaration of Competing Interest

The authors declare that they have no known competing financial interests or personal relationships that could have appeared to influence the work reported in this paper.

Data Availability

Data will be made available on request.

Acknowledgements

This study was financially supported by National Key Research and Development Program of China (2020YFC1807701), National Natural Science Foundation of China (42377256), Guizhou “Hundred” High-level Innovative Talent Project (GCC[2023]038) and complementary fund from the Guizhou Provincial Department of Science and Technology. Synchrotron based XAS analysis was conducted at Shanghai Synchrotron Radiation Facility on Beamline BL14W1.

Appendix A. Supporting information

Supplementary data associated with this article can be found in the online version at doi:10.1016/j.jhazmat.2024.134156.

References

[1] Ahmad, M., Lee, S.S., Lee, S.E., Al-Wabel, M.I., Tsang, D.C., Ok, Y.S., 2017. Biochar-induced changes in soil properties affected immobilization/mobilization of metals/metalloids in contaminated soils. J Soils Sediment 17, 717–730.
[2] Al-Jabban, W., Laue, J., Knutsson, S., Al-Ansari, N., 2019. Effect of disintegration times of the homogeneity of soil prior to treatment. Appl Sci 9 (22), 4791.
[3] Anderson, C.G., 2012. The metallurgy of antimony. Geochemistry 72, 3–8.
[4] Arrouays, D., Leenaars, J.G., Richer-de-Forges, A.C., Adhikari, K., Ballabio, C., Greve, M., et al., 2017. Soil legacy data rescue via GlobalSoilMap and other international and national initiatives. GeoResJ 14, 1–19.
[5] Bolan, N., Kumar, M., Singh, E., Kumar, A., Singh, L., Kumar, S., et al., 2022. Antimony contamination and its risk management in complex environmental settings: a review. Environ Int 158, 106908.
[6] Brady, N.C., Weil, R.R., 2002. The nature and properties of soils. J Range Manag 5 (6), 333.
[7] Cai, Y., Li, L., Wei, X., Zhang, G., Li, H., Fu, Z., 2012. Leaching experiments on the release of trace elements from tailings of Chashan antimony mine, Guangxi, China. Huanjing Kexue 33 (8), 2840–2848.
[8] Cassiani, G., Binley, A., Ferré, T., 2006. Unsaturated zone processes. Applied hydrogeophysics. Springer,, pp. 75–116.
[9] Chen, W., Liu, P., Luo, Y., Li, B., Peng, J., Jin, X., 2023. Behavior of Sb and As in the hydrogeochemistry of adjacent karst underground river systems and the responses of such systems to mining activities. Sci Total Environ 857, 159411.
[10] Chen, Z., Chen, Z., Feng, L., Yang, M., 2021. Rare earth element migration and impact of Dicranopteris dichotoma at mines in south China. Chemosphere 278, 130433.
[11] Cheng, H., Hu, Y., Luo, J., Xu, B., Zhao, J., 2009. Geochemical processes controlling fate and transport of arsenic in acid mine drainage (AMD) and natural systems. J Hazard Mater 165 (1-3), 13–26.
[12] Cornelis, G., Van Gerven, T., Snellings, R., Verbinnen, B., Elsen, J., Vandecasteele, C., 2011. Stability of pyrochlores in alkaline matrices: solubility of calcium antimonate. Appl Geochem 26 (5), 809–817.
[13] Demers, I., Molson, J., Bussière, B., Laflamme, D., 2013. Numerical modeling of contaminated neutral drainage from a waste-rock field test cell. Appl Geochem 33, 346–356.
[14] Deng, X., Huang, Y., Guo, Z., Mao, S., Li, S., Tong, L., et al., 2023. Reactive migration mechanism of Fe^{2+} and As^{3+} during groundwater discharge into river water: Insight from sand column experiments. J Hydrol 625, 130033.
[15] Ding, J., Zhang, Y., Ma, Y., Wang, Y., Zhang, J., Zhang, T., 2021. Metallogenic characteristics and resource potential of antimony in China. J Geochem Explor 230, 106834.
[16] Dittrich, M., Moreau, L., Gordon, J., Quazi, S., Palermo, C., Fulthorpe, R., et al., 2015. Geomicrobiology of iron layers in the sediment of Lake Superior. Aquat Geochem 21, 123–140.
[17] Duan, Y., Li, R., Gan, Y., Yu, K., Tong, J., Zeng, G., et al., 2020. Impact of physicochemical heterogeneity on arsenic sorption and reactive transport under water extraction. Environ Sci Technol 54 (23), 14974–14983.
[18] Dzombak, D.A., Morel, F.M., 1991. Surface complexation modeling: hydrous ferric oxide. John Wiley & Sons.
[19] U. EPA, 1996. Method 3052: Microwave assisted acid digestion of siliceous and organically based matrices. Revision 0.
[20] Fawcett, S.E., Jamieson, H.E., Nordstrom, D.K., McCleskey, R.B., 2015. Arsenic and antimony geochemistry of mine wastes, associated waters and sediments at the Giant Mine, Yellowknife, Northwest Territories, Canada. Appl Geochem 62, 3–17.
[21] Feng, Y., Liu, P., Wang, Y., Finfrock, Y.Z., Xie, X., Su, C., et al., 2020. Distribution and speciation of iron in Fe-modified biochars and its application in removal of As (V), As(III), Cr (VI), and Hg (II): An X-ray absorption study. J Hazard Mater 384, 121342.
[22] Filella, M., Philippo, S., Belzile, N., Chen, Y., Quentel, F., 2009. Natural attenuation processes applying to antimony: a study in the abandoned antimony mine in Goesdorf, Luxembourg. Sci Total Environ 407 (24), 6205–6216.
[23] Fuentes, E., Pinochet, H., De Gregori, I., Potin-Gautier, M., 2003. Redox speciation analysis of antimony in soil extracts by hydride generation atomic fluorescence spectrometry. Spectrochim Acta Part B: Spectrosc 58 (7), 1279–1289.
[24] Gill, L.W., Mac Mahon, J., Knappe, J., Morrissey, P., 2023. Hydraulic conductivity assessment of falling head percolation tests used for the design of on-site wastewater treatment systems. Water Res 236, 119968.
[25] Guo, X., Wang, K., He, M., Liu, Z., Yang, H., Li, S., 2014. Antimony smelting process generating solid wastes and dust: Characterization and leaching behaviors. J Environ Sci 26 (7), 1549–1556.
[26] He, Han, Z., Wu, F., Xiong, J., Gu, S., Wu, P., 2021. Spatial distribution and environmental risk of arsenic and antimony in soil around an antimony smelter of Qinglong County. Bull Environ Contam Toxicol 107 (6), 1043–1052.
[27] He, M., Wang, N., Long, X., Zhang, C., Ma, C., Zhong, Q., et al., 2019. Antimony speciation in the environment: recent advances in understanding the biogeochemical processes and ecological effects. J Environ Sci 75, 14–39.
[28] Hockmann, K., Tandy, S., Lenz, M., Schulin, R., 2014. Antimony leaching from contaminated soil under manganese-and iron-reducing conditions: column experiments. Environ Chem 11 (6), 624–631.
[29] Hu, X., He, M., Li, S., Guo, X., 2017. The leaching characteristics and changes in the leached layer of antimony-bearing ores from China. J Geochem Explor 176, 76–84.
[30] Jacques, D., Šimůnek, J., Mallants, D., Van Genuchten, M.T., 2008. Modelling coupled water flow, solute transport and geochemical reactions affecting heavy metal migration in a podzol soil. Geoderma 145 (3-4), 449–461.

[31] Jarvis, N., 2007. A review of non-equilibrium water flow and solute transport in soil macropores: principles, controlling factors and consequences for water quality. Eur J Soil Sci 58 (3), 523–546.
[32] Johnston, S.G., Bennett, W.W., Doriean, N., Hockmann, K., Karimian, N., Burton, E. D., 2020. Antimony and arsenic speciation, redox-cycling and contrasting mobility in a mining-impacted river system. Sci Total Environ 710, 136354.
[33] Kong, L., Hu, X., He, M., 2015. Mechanisms of Sb (III) oxidation by pyrite-induced hydroxyl radicals and hydrogen peroxide. Environ Sci Technol 49 (6), 3499–3505.
[34] Lee, S.-H., Tanaka, M., Takahashi, Y., Kim, K.-W., 2018. Enhanced adsorption of arsenate and antimonate by calcined Mg/Al layered double hydroxide: Investigation of comparative adsorption mechanism by surface characterization. Chemosphere 211, 903–911.
[35] Luo, G., Han, Z., Xiong, J., He, Y., Liao, J., Wu, P., 2021. Heavy metal pollution and ecological risk assessment of tailings in the Qinglong Dachang antimony mine, China. Environ Sci Pollut Res 28, 33491–33504.
[36] Majzlan, J., Števko, M., Lánczos, T., 2016. Soluble secondary minerals of antimony in Pezinok and Kremnica (Slovakia) and the question of mobility or immobility of antimony in mine waters. Environ Chem 13 (6), 927–935.
[37] Mayer, K., Benner, S., Blowes, D., Frind, E., 1999. The reactive transport model MIN3P: application to acid mine drainage generation and treatment-nickel rim mine site, Sudbury, Ontario. Min Environ 1, 145–154.
[38] McKeague, J., 1978. Manual on soil sampling and methods of analysis. Can Soc Soil Sci.
[39] Ni, Y., Ou, Z., Ying, P., 2001. Preferential flow and its effect on solute migration in soil. J Appl Ecol 12 (1), 103–107.
[40] Osunbitan, J., Oyedele, D., Adekalu, K., 2005. Tillage effects on bulk density, hydraulic conductivity and strength of a loamy sand soil in southwestern Nigeria. Soil Tillage Res 82 (1), 57–64.
[41] Pabst, T., Molson, J., Aubertin, M., Bussière, B., 2017. Reactive transport modelling of the hydro-geochemical behaviour of partially oxidized acid-generating mine tailings with a monolayer cover. Appl Geochem 78, 219–233.
[42] Palmer, M.J., Chételat, J., Richardson, M., Jamieson, H.E., Galloway, J.M., 2019. Seasonal variation of arsenic and antimony in surface waters of small subarctic lakes impacted by legacy mining pollution near Yellowknife, NT, Canada. Sci Total Environ 684, 326–339.
[43] Prommer, H., Sun, J., Kocar, B.D., 2019. Using reactive transport models to quantify and predict groundwater quality. Elem: Int Mag Mineral, Geochem, Petrol 15 (2), 87–92.
[44] Purandara, B., Sujitha, V., Shivapur, A.V., Tyagi, J., 2021. Modelling of soil moisture movement and solute transport in parts of Malaprabha Command. J Geol Soc India 97, 293–296.
[45] Qi, P., Pichler, T., 2016. Sequential and simultaneous adsorption of Sb(III) and Sb (V) on ferrihydrite: Implications for oxidation and competition. Chemosphere 145, 55–60.
[46] Qi, P., Pichler, T., 2017. Competitive adsorption of As(III), As(V), Sb(III) and Sb(V) onto ferrihydrite in multi-component systems: Implications for mobility and distribution. J Hazard Mater 330, 142–148.
[47] Ravel, B., Newville, M., 2005. ATHENA, ARTEMIS, HEPHAESTUS: data analysis for X-ray absorption spectroscopy using IFEFFIT. J Synchrotron Radiat 12 (4), 537–541.
[48] Rawson, J., Siade, A., Sun, J., Neidhardt, H., Berg, M., Prommer, H., 2017. Quantifying Reactive Transport Processes Governing Arsenic Mobility after Injection of Reactive Organic Carbon into a Bengal Delta Aquifer. Environ Sci Technol 51 (15), 8471–8480.
[49] Ren, W., Ran, Y., Mou, Y., Cui, Y., Sun, B., Yu, L., et al., 2023. Pollution characteristics and risk assessment of antimony and arsenic in a typical abandoned antimony smelter. Environ Geochem Health 1–14.
[50] Rong, Q., Zhang, C., Huang, H., Li, C., Nong, X., Zhao, H., et al., 2021. Immobilization of As and Sb by combined applications Fe–Mn oxides with organic amendments and alleviation their uptake by Brassica campestris L. J Clean Prod 288, 125088.
[51] Simunek, J. , Sejna, M. , Van Genuchten, M.T. , Šimůnek, J. , Šejna, M. , Jacques, D. , et al. , 1998. HYDRUS-1D. Simulating the one-dimensional movement of water, heat, and multiple solutes in variably-saturated media, version 2.
[52] Su, D., Mayer, K.U., MacQuarrie, K.T., 2021. MIN3P-HPC: a high-performance unstructured grid code for subsurface flow and reactive transport simulation. Math Geosci 53, 517–550.
[53] Sun, J., Chillrud, S.N., Mailloux, B.J., Bostick, B.C., 2016. In situ magnetite formation and long-term arsenic immobilization under advective flow conditions. Environ Sci Technol 50 (18), 10162–10171.
[54] Sun, J., Prommer, H., Siade, A.J., Chillrud, S.N., Mailloux, B.J., Bostick, B.C., 2018. Model-based analysis of arsenic immobilization via iron mineral transformation under advective flows. Environ Sci Technol 52 (16), 9243–9253.
[55] Sun, J., Quicksall, A.N., Chillrud, S.N., Mailloux, B.J., Bostick, B.C., 2016. Arsenic mobilization from sediments in microcosms under sulfate reduction. Chemosphere 153, 254–261.
[56] Wallis, I., Prommer, H., Berg, M., Siade, A.J., Sun, J., Kipfer, R., 2020. The river–groundwater interface as a hotspot for arsenic release. Nat Geosci 13 (4), 288–295.
[57] Wang, W., Dai, X., Guo, W., Jin, L., Hu, S., 2020. Field-based speciation of inorganic Sb using ion-exchange resin cartridge and ICP-MS detection. Spectrosc 41 (2), 74–80.
[58] Welter, D.E., White, J.T., Hunt, R.J., Doherty, J.E., 2015. Approaches in highly parameterized inversion—PEST++ Version 3, a Parameter ESTimation and uncertainty analysis software suite optimized for large environmental models. US Geological Survey.
[59] Wenzel, W.W., Kirchbaumer, N., Prohaska, T., Stingeder, G., Lombi, E., Adriano, D. C., 2001. Arsenic fractionation in soils using an improved sequential extraction procedure. Anal Chim Acta 436 (2), 309–323.
[60] Wilson, S.C., Lockwood, P.V., Ashley, P.M., Tighe, M., 2010. The chemistry and behaviour of antimony in the soil environment with comparisons to arsenic: a critical review. Environ Pollut 158 (5), 1169–1181.
[61] Xie, X., Gu, S., Hao, L., Zhang, T., Guo, Z., 2022. Rhizosphere microbial communities and geochemical constraining mechanism of antimony mine waste-adapted plants in southwestern china. Microorganisms 10 (8), 1507.
[62] You, X., Liu, S., Dai, C., Guo, Y., Zhong, G., Duan, Y., 2020. Contaminant occurrence and migration between high- and low-permeability zones in groundwater systems: A review. Sci Total Environ 743, 140703.
[63] Zeng, H., Gu, S., 2017. Environmental quality assessment on karst groundwater in antimony and coal mines concentration area of qinglong. Environ Monit China 33, 78–86.
[64] Zeng, J., Li, C., Wang, J., Tang, L., Wu, C., Xue, S., 2022. Pollution simulation and remediation strategy of a zinc smelting site based on multi-source information. J Hazard Mater 433, 128774.
[65] Zhang, H., Li, L., Zhou, S., 2014. Kinetic modeling of antimony (V) adsorption–desorption and transport in soils. Chemosphere 111, 434–440.
[66] Zhang, X., Ma, F., Yin, S., Wallace, C.D., Soltanian, M.R., Dai, Z., et al., 2021. Application of upscaling methods for fluid flow and mass transport in multi-scale heterogeneous media: A critical review. Appl Energy 303, 117603.
[67] Zhang, Y., O'Loughlin, E.J., Kwon, M.J., 2022. Antimony redox processes in the environment: a critical review of associated oxidants and reductants. J Hazard Mater 431, 128607.
[68] Zhao, L., Shangguan, Y., Yao, N., Sun, Z., Ma, J., Hou, H., 2020. Soil migration of antimony and arsenic facilitated by colloids in lysimeter studies. Sci Total Environ 728, 138874.
[69] Zhao, Xp, Yang, B., Li, C., Ren, W., Zhao, P., Gu, X., 2023. Species distribution and geochemical modeling of antimony in the Qinlong antimony mining area. Environ Chem 1–9.
[70] Zheng, L., Chen, W., Jia, S., Wu, L., Zhong, B., Liao, W., et al., 2020. Temporal and spatial patterns of nitrogen wet deposition in different weather types in the Pearl River Delta (PRD), China. Sci Total Environ 740, 139936.
[71] Zhou, J., Nyirenda, M.T., Xie, L., Li, Y., Zhou, B., Zhu, Y., et al., 2017. Mine waste acidic potential and distribution of antimony and arsenic in waters of the Xikuangshan mine, China. Appl Geochem 77, 52–61.
[72] Zhou, Z., Liu, P., Wang, S., Finfrock, Y.Z., Ye, Z., Feng, Y., et al., 2022. Iron-modified biochar-based bilayer permeable reactive barrier for Cr(VI) removal. J Hazard Mater 439, 129636.